Bistable swirled flames and influence on flame transfer functions

Sebastian Hermeth, Gabriel Staffelbach, Laurent Y.M. Gicquel, Vyacheslav Anisimov, Cinzia Cirigliano, Thierry Poinsot

Bistable swirled flames and influence on flame transfer functions

Sebastian Hermeth [a,*], Gabriel Staffelbach [a], Laurent Y.M. Gicquel [a], Vyacheslav Anisimov [b], Cinzia Cirigliano [b], Thierry Poinsot [c]

[a] CERFACS, 42 Avenue G. Coriolis, 31057 Toulouse Cedex, France
[b] Ansaldo Energia S.p.A, Via N. Lorenzi, 8, 16152 Genoa, Italy
[c] Institut de Mécanique des Fluides de Toulouse, Avenue C. Soula, 31400 Toulouse, France

Keywords:
Combustion
Thermo-acoustic instabilities
Large eddy simulations

A B S T R A C T

Large Eddy Simulations (LES) are used to study a lean swirl-stabilized gas turbine burner where the flow exhibits two stable states. In the first one, the flame is attached to the central bluff body upstream of the central recirculation zone which contains burnt gases. In the second one the flame is detached from the central bluff body downecirculation zone which is filled by cold unburnt gases and dominated by a strong Precessing Vortex Core (PVC). The existence of these two states has an important effect on the dynamic response of the flame (FTF): both gain and phase of the FTF change significantly in the detached case compared to the attached one, suggesting that the stability of the machine to thermoacoustic oscillations will differ, depending on the flame state. Bifurcation diagrams show that the detached flame cannot be brought back to an attached position with an increased fuel flow rate, but it can be re-attached by forcing it at high amplitudes. The attached flame however, behaves inversely: it can be brought back to the detached position by both decreasing or increasing the pilot mass flow rate, but it remains attached at all forcing amplitudes.

1. Introduction

Swirling flows are commonly used to help flame stabilization in gas turbine combustion chambers. They feature several types of vortex breakdown and can exhibit bifurcation phenomena where different states can co-exist and the flow can jump spontaneously from one to another [1,2]. Bifurcations of flames in configurations which are close to real gas turbine chambers have not been investigated so far even though engineers report that they observe these mechanisms and that there is a link between flame states and thermoacoustic instabilities: when the flame changes from one state to another, its acoustic stability characteristics also change.

Two dynamic phenomena are usually observed in swirled combustion chambers: (1) a helical flow instability, the so-called precessing vortex core (PVC) and (2) thermo-acoustic instabilites.

The PVC is an hydrodynamic instability in swirling flows [3]. It is a large scale structure characterized by a regular rotation of a spiral structure around the geometrical axis of the combustion chamber. It can occur at high Reynolds and swirl number flows [4–10] and its precession frequency is controlled by the rotation rate of the swirled flow [3]. Several studies show that combustion can suppress the PVC [6,7,11], but other cases also show PVCs which are present in reacting flows [12–15]. The interaction of PVC with flames has been analyzed for example by Stöhr et al. [16]: they found the PVC to enhance mixing and to increase the flame surface. This was associated to structures in the inner shear layer, whereas Moeck et al. [15] observed the outer shear layer to create most of the flame perturbations. Both researchers as well as Staffelbach [13] using LES evidenced a "finger-like" rotating structure at the flame foot around which the PVC is turning. Furthermore, asymmetric fluctuations of the heat release rate are usually associated to the rotating PVC [12,15].

A second phenomenon present in todays low-emission gas turbines is thermo-acoustic instabilities [17]. They are due to a resonant coupling of the unsteady heat release and the acoustics propagating in the system and their prediction has become an important task to prevent their appearance at an early design stage [18–20]. For acoustically compact flames the linear analysis of combustion instabilities is generally performed with the Flame Transfer Function (FTF) introduced by Crocco [21,22] and more recently with the Flame Describing Function (FDF) [23,24]. In these approaches the FTF is defined as the relative heat release fluctuation $(\hat{q}/\bar{q})$ to the relative inlet velocity perturbation $(\hat{u}/\bar{u})$ induced by the acoustic field:

$$F(\omega) = \frac{\hat{q}/\bar{q}}{\hat{u}/\bar{u}} = ne^{-i\phi(\omega)} \quad (1)$$

* Corresponding author. Address: CERFACS, CFD Team, 42 Avenue G. Coriolis, 31057 Toulouse Cedex 01, France. Fax: +33 (0)5 61 19 30 00.
E-mail address: hermeth@cerfacs.fr (S. Hermeth).

The $F(\omega)$ function is generally expressed in the frequency domain as amplitude n and phase $\phi(\omega)$ which are functions of the forcing frequency ω (and forcing amplitude for FDFs). It is affected by different mechanisms acting simultaneously on the heat release rate fluctuation and therefore difficult to separate [25]: the axial velocity perturbation [26–29], the perturbation of swirl [30–34] and the perturbation of mixing [35–38]. The gain of FTFs for swirled flames exhibits a typical shape: it starts at 1, then increases towards a maximum, decreases to a local minimum at low frequencies, often reaches a second maximum at higher frequencies and decreases finally to low values at high frequencies. The FTF phase evolves in a quasi-linear way [29,33,34,39].

Both phenomena, the PVC and combustion instabilities, can be simultaneously present in swirled flames and interact with each other but the link between PVC and thermoacoustics remains a controversial issue. Several studies [40,11,10] have shown that the PVC can provoke thermo-acoustic instabilities because the flame position and the recirculation zones change when the PVC is active [10,14]. Forced acoustic oscillations can also lead to a stretching and contracting of the PVC [41]. Moreover, Paschereit et al. [12] observed that low amplitude forcing can suppress the PVC, and Moeck et al. [15] found the same effect but at high oscillation amplitudes.

The aim of this paper is to show that the link between PVC and thermoacoustics can take a different form: the swirled flow leading to the existence of a PVC can be bistable, leading to the existence of two states for the same regime. These two states have very different mean flows but also different FTFs so that one of them may lead to a thermoacoustic oscillation and not the other. This is shown by Tay and Polifke [42]: dependent on the thermal wall boundary conditions used, two different flames with different FTFs are present in the same configuration. In this paper however, it is shown that two different flames and FTFs can exist for exactly the same operating conditions. Moreover, the bistable nature of the swirled flow makes even FTF studies complicated: the flame can switch from a state to another when the mean fuel flow rate injected in the pilot flame is varied but also when the flame is forced acoustically to measure FTFs because these forced oscillations can be strong enough to trigger bifurcations. These phenomena are studied here in one specific example of gas turbine chamber using LES. For this chamber, the existence of two states for the same regime was revealed by LES. In the first state, the flame is attached to the burner and the PVC is suppressed, whereas in the second one, the flame is detached from the burner and separated from the burner outlet by a strong PVC.

The target configuration is first described (Section 2) and the LES-solver, mesh and boundary conditions are presented (Section 3). The LES is validated against experiments in Section 4 in terms of flow fields and pressure drop for the cold flow on an atmospheric test rig. Section 5 shows how the LES is initialized in order to obtain two different flames at the same operating point and Section 6 compares the LES results for mean and instantaneous flow fields. The dynamic response of both flames to an acoustic perturbation is analyzed for different forcing frequencies in Section 7. Bifurcation diagrams are constructed in Section 8 to study the effect of the mean fuel flow rate on re-attachment and detachment process of both flames. Finally, different forcing amplitudes at one frequency are studied and hysteresis and an eventual suppression of the PVC are discussed (Section 9).

2. Target configuration

The burner considered here is a hybrid burner operated at high pressure possessing multiple air and fuel inlets (Fig. 1). Air is injected through two coaxial swirlers (diagonal and axial) with the main air mass flow passing through the diagonal passage. Methane is injected through small holes in the vanes of the diagonal passage and mixes with air before reaching the combustion chamber where the flame stabilizes due to vortex breakdown [2,43]. To help flame stabilization in this lean combustor a pilot methane injection is added in the axial part of the injection system. Cooling air inlets are also present to shield the Cylindrical Burner Outlet (CBO) and the center bluff body, seen on Fig. 1.

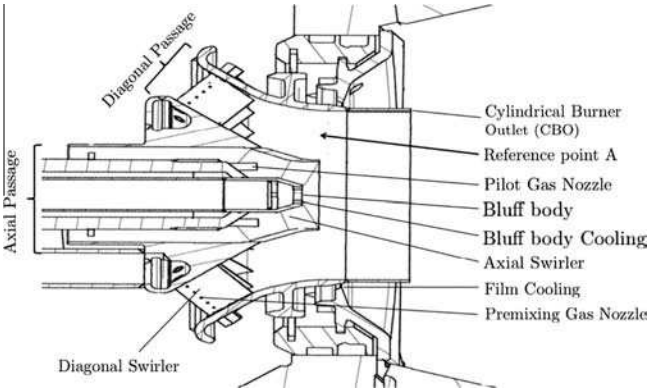

Fig. 1. Burner details and reference point A (proportions changed).

Two configurations were used here:

- Experimental test rig for cold flow validation
  Large-Eddy Simulation was first validated against experiments performed on a test rig at atmospheric pressure. In this specific laboratory experiment installed in Ansaldo Energia S.p.A, a single burner is mounted on a octagonal combustion chamber as shown in Fig. 2. Only air is injected through the diagonal and axial swirler and the results are used to validate LES prediction for pressure losses through the burner as well as velocity profiles.
- Real gas turbine
  In the real gas turbine, the burner is mounted on a section of an annular combustion chamber. This section is used as the computational domain retained for LES (Fig. 3). The use of a single sector LES instead of a full annular LES is justified by the ISAAC assumption assuming that azimuthal modes mainly induce longitudinal fluctuations in each burner and can thus be studied on a single sector [44,45].

3. Large eddy simulation

LES is well suited to unsteady combustion and is a useful tool to predict thermoacoustic limit cycles or FTFs [17,32,20]. The LES solver is described in Section 3.1, and the mesh and boundary conditions are given in Sections 3.2 and 3.3, respectively.

3.1. LES solver

The LES code is a fully compressible explicit solver using a cell-vertex approximation for the reactive multi-species Navier–Stokes equations on unstructured grids [46]. The viscous stress tensor, the heat diffusion vector and the species molecular transport use classical gradient approaches. The fluid viscosity follows the Sutherland law and the species diffusion coefficients are obtained using a constant species Schmidt number and diffusion velocity corrections for mass conservation. A second-order finite element scheme is used for both time and space advancement [47,48]. The Sub-grid stress tensor is modeled by the classical Smagorinsky model [49]. Chemistry is computed using a two-step mechanism for methane/air flames [50] which includes two reactions and six species (CH_4, O_2, CO_2, CO, H_2O and N_2). The first reaction is irreversible

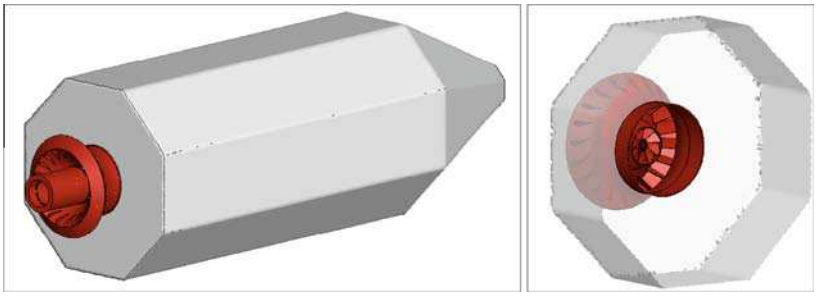

Fig. 2. The single burner installed in Ansaldo Energia S.p.A on a laboratory chamber for cold flow experiments.

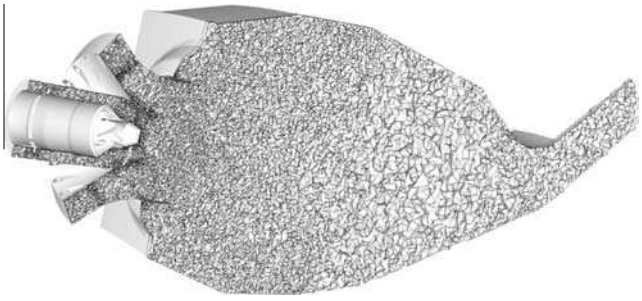

Fig. 3. Mesh details on middle cut plane.

and controls the oxydation of CH_4, while the second reaction is reversible leading to an equilibrium between CO and CO_2 [6].

$$CH_4 + \frac{3}{2}O_2 \rightarrow CO + 2H_2O \tag{2}$$

$$CO + \frac{1}{2}O_2 \leftrightarrow CO_2 \tag{3}$$

The first reaction rate q_1 is described by:

$$q_1 = A_1 \left(\frac{\rho Y_{CH_4}}{W_{CH4}}\right)^{n_1^{CH_4}} \left(\frac{\rho Y_{O_2}}{W_{O_2}}\right)^{n_1^{O_2}} exp\left(-\frac{E_{a1}}{RT}\right) \tag{4}$$

while the second reaction rate q_2 is given by:

$$q_2 = A_2 \left[\left(\frac{\rho Y_{CO}}{W_{CO}}\right)^{n_2^{CO}} \left(\frac{\rho Y_{O_2}}{W_{O_2}}\right)^{n_2^{O_2}} \left(\frac{\rho Y_{CO_2}}{W_{CO_2}}\right)^{n_2^{CO_2}}\right] exp\left(-\frac{E_{a2}}{RT}\right) \tag{5}$$

This scheme was developed and fitted to match the full mechanism's behavior for the considered equivalence ratios [50]. The Arrhenius rate parameters are all given in [50] and were used without any change. To capture flame/turbulence interactions, the dynamic thickened flame model is used [51–53] and is well suited for all flames studied here which correspond to premixed or partially premixed regimes. Sub-grid scale wrinkling and interactions are modeled using the efficiency function [51–54].

3.2. Mesh

LES are performed on a fully unstructured mesh of 895,196 nodes and 4,655,880 tetrahedral elements for the experimental cold flow set-up (Fig. 2) and 1,921,370 nodes and 10,472,070 tetrahedral elements for the real gas turbine (Fig. 3). The mesh is kept similar in the burner for the real gas turbine and the experimental test rig in order to validate it in terms of pressure loss and velocity components. The time step is 1.2×10^{-7} s and 9×10^{-8} s for the experimental test rig and the real gas turbine, respectively, corresponding to an acoustic CFL number equal to 0.7 [55]. The mesh is refined in the flame region and in the vicinity of the fuel injection. Although mesh dependency is a critical aspect of LES for complex burners, full mesh convergence is clearly out of reach today for this real industrial gas turbine burner considering the actual size and flow Reynolds number: here, we will compare LES results with experiments for cold conditions and rely on multiple previous computations performed with AVBP to verify mesh effect in reacting cases [56,57].

3.3. Boundary conditions

Inlet and outlet boundary conditions are imposed through the Navier–Stokes Characteristic Boundary Condition (NSCBC) formulation [58] to control acoustic reflection on boundaries by the use of a reflection coefficient. The NSCBC boundaries behave like a first-order low-pass filter and have cut-off frequencies proportional to the relaxation coefficient. All walls are modeled using a logarithmic wall-law condition [59] and side boundaries of the combustion chamber are considered axi-periodic.

Forcing is introduced by generating a harmonic acoustic perturbation at the diagonal inlet using the inlet wave modulation method [60]. The response of the flame is quantified by measuring the perturbation of the heat release rate. The velocity signal for FTF quantification is measured at the reference point A (Fig. 1). The four forcing frequencies $f_1 < f_2 < f_3 < f_4$ correspond to critical frequencies in the real chamber. It was checked that the NSCBC conditions behave almost non-reflecting in this frequency range. The FTF for the four frequencies is obtained with a forcing amplitude of 6 percent of the mean inlet velocity to ensure linearity. Six cycles of oscillation are used to identify the FTF. Tests have been performed to investigate the effect of pulsating the diagonal or axial passages separately. Pulsating only the diagonal swirler results in the same flame response as pulsating both axial and diagonal passages, so that only the first is discussed here. In order to study bifurcation, the pulsation amplitude at frequency f_4 is varied from 15 to 45 percent of the mean inlet velocity in Section 9.

4. Non-reacting flow fields

In the absence of experimental results for the high pressure combustion chamber, LES was validated on an atmospheric test rig where experiments have been carried out. The Reynolds number in the combustion chamber (based on the burner diameter and the bulk velocity) is of the order of 1,000,000. For such high Reynolds number flows, the validation of LES is difficult. Performing experimental measurements is also much more difficult than in lab-scale set-ups. Cold flow LES is validated here against PIV and pressure drop measurements through the burner.

For this swirler with multiple passages, the flow topology is more complicated than in usual swirling flows. Here, two recirculation zones are found on the chamber axis (Fig. 4). As indicated by the zero velocity iso-lines, negative velocity occurs first close to the

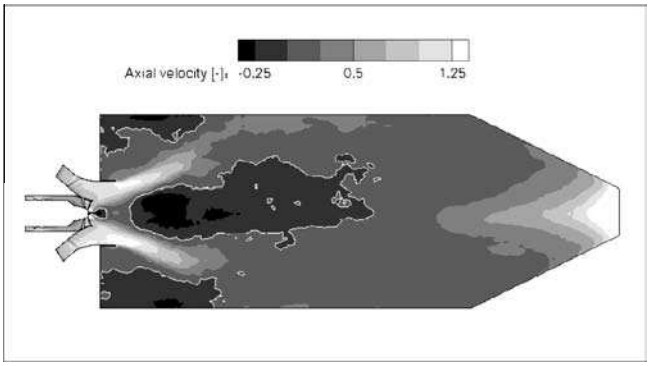

Fig. 4. Mean axial velocity field on middle cut plane. The white line corresponds to zero axial velocity.

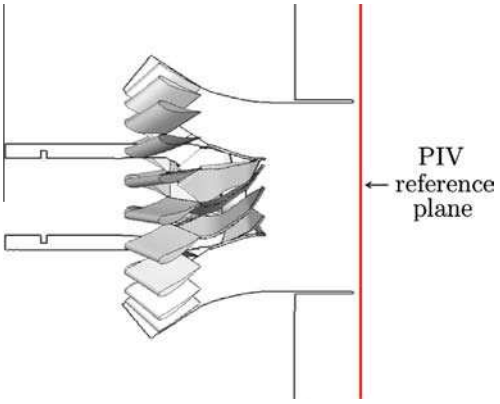

Fig. 5. Reference plane location and position of profile extraction.

bluff body followed by a region of positive velocity and finally by the main inner recirculation zone. All velocities are non-dimensionalized by the bulk velocity. LES and PIV experiments are compared in Fig. 6 for the axial velocity on the measurement plane (Fig. 5) just in front of the burner outlet: in the center LES predicts low positive values, but PIV show low negative axial velocities. From the center to the CBO in radial direction, the axial velocity increases significantly with a similar amplitude between PIV and LES. Note that experiments were not performed everywhere: points without PIV data are marked as zero velocities. The velocities in y- and z directions are compared in Figs. 7 and 8, respectively. Experiments and LES agree: the y-velocity is maximal in magnitude on the upper and lower sides with opposite sign. The positions of peaks and zero velocities are in good agreement for both velocity components. Furthermore, similar tangential velocity (u_{tang}) fields are found (Fig. 9). The u_{tang} velocity is calculated as the cross-product of the velocity vector in the radial direction:

$$U_{tang} = \frac{v \times r}{|r|} \tag{6}$$

The lowest velocity is found in the center and increases in the radial direction. LES slightly under predicts the magnitude in the outer region and predicts an almost uniform distribution at fixed radius, whereas PIV shows a higher velocity magnitude in the top and bottom regions. Profiles of the four velocity components U_{ax}, U_y, U_z and U_{tang} (cut in Fig. 5) are shown in Fig. 10 and LES and experiments agree overall, but differences occur in the inner recirculation zone. The instantaneous flow fields confirm the existence of a PVC in the cold flow. It is characterized by a regular rotation of a spiral structure around the geometrical axis of the combustion chamber (Fig. 11) for one cycle. The frequency predicted by LES matches the one observed in the experiment by Razore S. with an error margin of 20% (internal report) which is typical in these devices. It corresponds to a Strouhal $St = fD/u_{bulk} = 1.3$ based on the burner diameter D and the bulk velocity u_{bulk}.

Another possibility to evaluate the quality of LES is to compare the pressure drop through the burner against measurements. A convenient way to quantify pressure losses is to introduce an equivalent section S_e defined by

$$S_e = \frac{\dot{m}}{\sqrt{2(p_{in} - p_c)\rho}} \tag{7}$$

where p_{in} and p_c denote the total pressure at the inlet of the considered passage and in the chamber, respectively. The averaged total pressure field (normalized by the mean value in the chamber) is given in Fig. 12 and shows a low pressure region in front of the bluff body due to the rotating PVC. The chamber pressure is taken for three different points: P1–P3 (Fig. 12). For those points the static pressure is almost identical to the total pressure as they are located in low speed zones. The inlet pressure is calculated by mass weighted averaging the corresponding inlet patch for both diagonal and axial swirlers. Experimental and LES results are compared in Table 1. The static pressure in the chamber does not change much so that all points give similar results: the equivalent sections for both swirler passages agree well with the experiments showing an error margin less than 2.0%.

5. Initialisation of the reacting LES

LES reveals that when the computing parameters are changed from one operating point (1) to another one (2) (Fig. 13), the flame can stabilize in different ways depending on the transition between the two states. This happens only for certain operating conditions: operating point 2 is characterized by a higher chamber

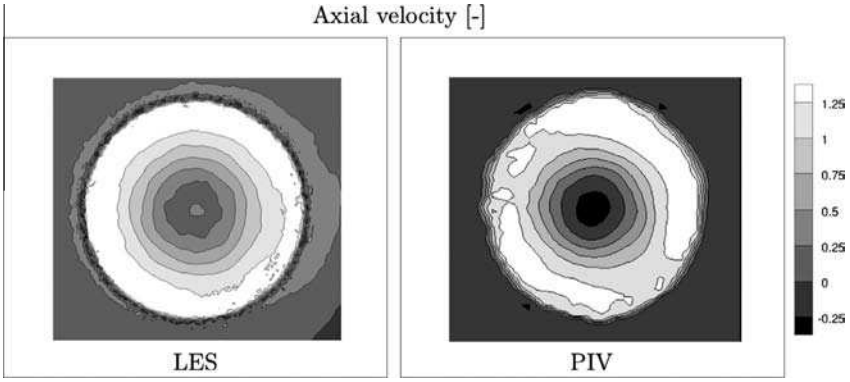

Fig. 6. Axial-velocity: comparison PIV and LES.

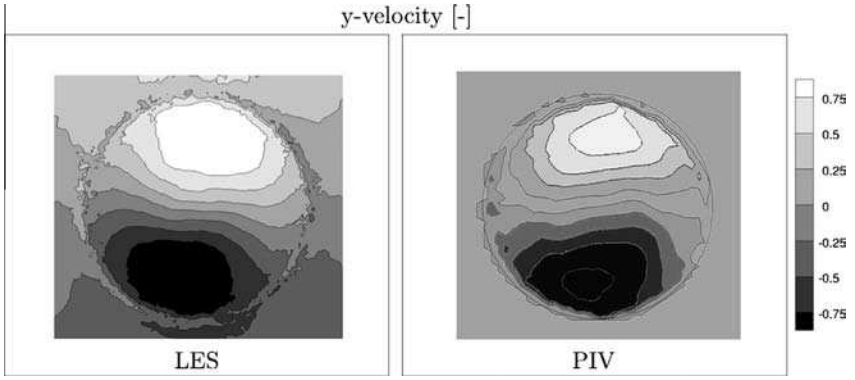

Fig. 7. *y*-velocity: comparison PIV and LES.

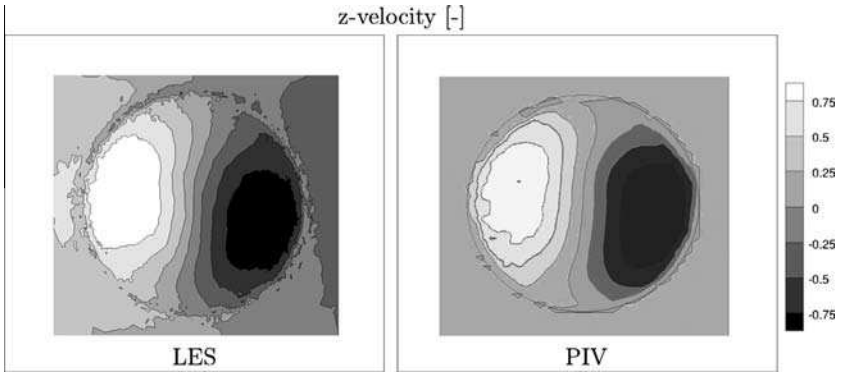

Fig. 8. *z*-velocity: comparison PIV and LES.

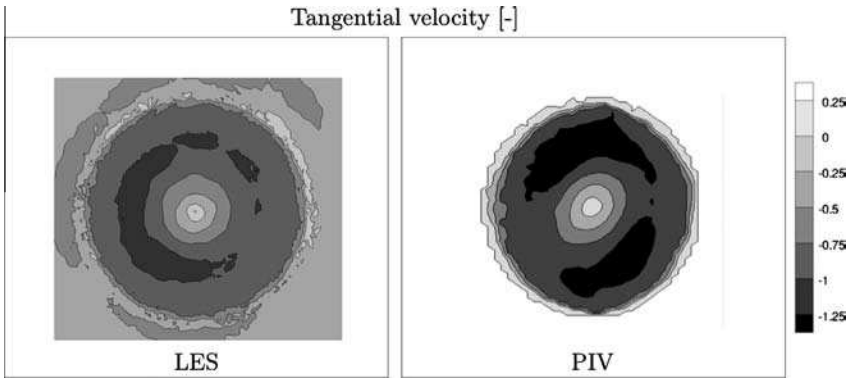

Fig. 9. Tangential velocity: comparison PIV and LES.

pressure ($p_2 > p_1$), a lower compressor outlet temperature ($T_2 < T_1$), higher air mass flow rates at the diagonal ($\dot{m}_{Diag,Air,2} > \dot{m}_{Diag,Air,1}$) and the axial inlet ($\dot{m}_{Axial,Air,2} > \dot{m}_{Axial,Air,1}$) as well as higher fuel flow rates in the premixing gas nozzle ($\dot{m}_{Diag,Fuel,2} > \dot{m}_{Diag,Fuel,1}$) and the pilot nozzle ($\dot{m}_{Axial,Fuel,2} > \dot{m}_{Axial,Fuel,1}$). Operating point 1, where the flame is stabilized at the bluff body and no PVC appears, is used as initialisation for the LES. When the transition is applied rapidly, meaning that all boundary conditions are set to condition 2 simultaneously ($\{\dots\}_{BC} = \{\dots\}_2$), the flame detaches from the bluff body (path 1 in Fig. 13). On the other hand, when the boundary conditions are changed slowly by first doubling the pilot fuel (2a in Fig. 13), then changing the pressure (2b) followed by adapting the air mass flow rates and the fuel flow rate in the premixing gas nozzle (2c) and finally reducing the pilot mass flow rate to condition 2, the flame remains attached to the bluff body. This means that two stable positions can exist for exactly the same operating point: the flame is bi-stable. The resulting flow fields are analyzed in details in the next section. For simplicity reasons the nomenclature listed in Table 2 is used for both the attached and the detached flame under operating conditions 2.

6. Analysis of the steady flame states

6.1. Mean flow fields

The topology of both states can be visualized by plotting the three-dimensional surface of the averaged flame (Fig. 14) where the flame surface is visualized by a temperature iso-surface ($T/T_{mean} = 1.3$) colored by the normalized axial velocity. All velocities

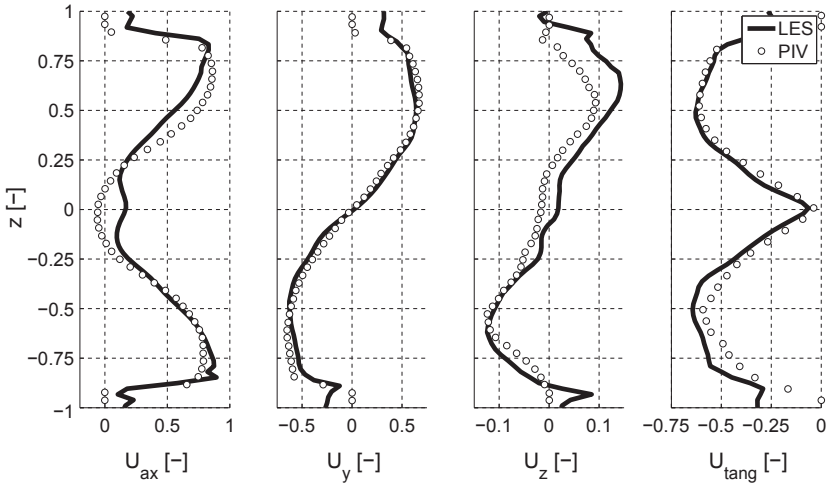

Fig. 10. Comparison of PIV and LES results on the reference cut (Fig. 5) for U_{ax}, U_y, U_z and U_{tang}.

Fig. 11. Precessing vortex core (PVC) in cold flow LES visualized as a low pressure iso-surface.

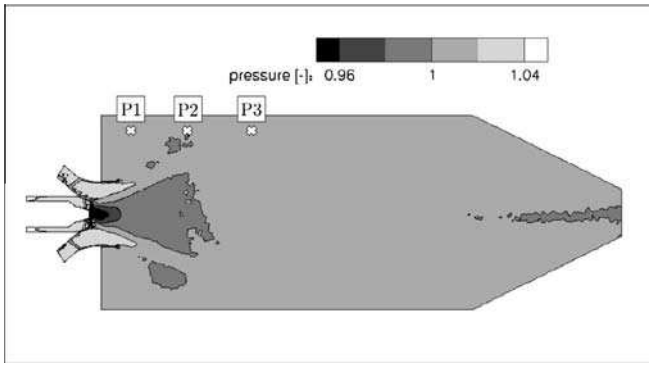

Fig. 12. Total pressure field on middle cut plane.

Table 1
Ratio S_e^{LES}/S_e^{Exp} of the computed equivalent section to the experimental value.

	Point 1	Point 2	Point 3
Diagonal swirler (%)	101.0	100.5	101.6
Axial swirler (%)	100.1	100.1	100.1

are non-dimensionalized by the bulk velocity and all other parameters by their mean value. The Reynolds number of the flow at the burner exit (based on the bulk flow and the burner injection system diameter) is 1.42×10^6. The Damköhler number was estimated from the ratio of the flow time (time required to go across the combustor at the bulk velocity) and the flame time (the ratio of the flame thickness to the flame speed estimated at the mean equivalence ratio of the burner). It leads to a Damköhler number of 3.37.

A cut through the middle plane reveals differences in the heat release field between both states (Fig. 15). Since the flame is detached from the bluff body, the high temperature, and therefore heat release, region around the pilot injection disappears for the *Detached* state. In this case the inner recirculation zone does not reach the bluff body (Fig. 16) and does not bring the flame back to the bluff body. Furthermore the recirculation zone of the *Attached* flame creates a geometrical contraction at the outlet of the burner accelerating the flow and leading to higher axial velocities. This is illustrated by plotting the axial velocity along seven cuts (shown in Fig. 17) in Fig. 18. The *Attached* flame shows significantly higher velocities along the flame region (cut 2 to 7). The *Detached* flame shows almost no recirculation flow close to the bluff body and a positive axial velocity in the inner region (cut 1 to 3), whereas the recirculation zone of the *Attached* case leads to negative velocities. In the inner recirculation zone from cut 4 on, both velocity fields become similar. The radial velocity profiles in Fig. 19 reveal further differences. The magnitude of the radial velocity is defined as the dot product of the velocity vector in the radial direction:

$$U_{rad} = \frac{v \cdot r}{|r|} \tag{8}$$

On the first cut 1, low radial velocities appear in *Detached* in the inner region where *Attached* shows important peaks. In the outer region both profiles are similar. Up to location 5 both profiles are similar in terms of position and magnitude of extrema. At 6 and 7 the *Detached* flow is more expanded than in the *Attached* one. Further differences are visible for the tangential velocity profiles in Fig. 20. Close to the bluff body (1 and 2), significantly higher velocities are found in *Detached* in the inner region, where the peak has a larger extent than in *Attached*. Further outside the *Detached* peak meets the *Attached* one and both cases match in the outer region. Strong velocity fluctuations appear close to the bluff body for *Detached* as evidenced by the turbulent kinetic energy $k = 1/2(u'^2 + v'^2 + w'^2)$ fields displayed in Fig. 21. This peak decreases downstream and almost vanishes when reaching the flame. On the other hand the inner recirculation zone in *Attached* has low

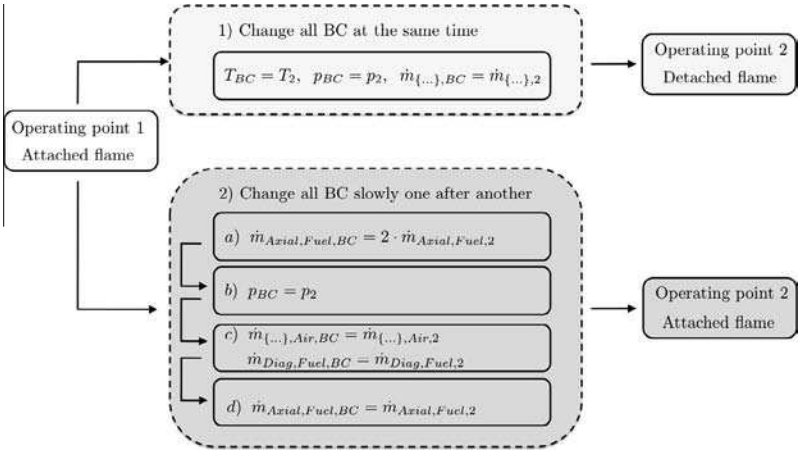

Fig. 13. Initialisation of operating point 2. Starting point is operating condition 1 where the flame is stabilized at the bluff body (attached). Depending on the transition between the two states, the flame can detach (option 1) or stay attached (option 2).

Table 2
Nomenclature for attached and detached flame.

Attached	The flame is attached at the bluff body
Detached	The flame is detached from the bluff body

velocity fluctuations, but they are high in the shear layer at the outlet of the diagonal swirler (3 and 4).

The differences between the two flame states can be visualized using temperature profiles (Fig. 22). The maximum temperature is higher for *Attached*. The recirculation zone is weak and cold for *Detached*, while it is strong and hot for *Attached*. The *Detached* flame shows no peak in the central zone for the first profiles (1 to 4), but starts to develop one at 6. The flame lengths are similar in both states and an almost constant temperature profile is reached at position 7. The *Detached* flame exhibits temperature fluctuations (Fig. 23) over a wider radial range suggesting that NO production would also be different for both states. Figures 18–22 confirm that the *Attached* state is characterized by a hot recirculation zone, while the *Detached* state has no hot gases in its central recirculation zone.

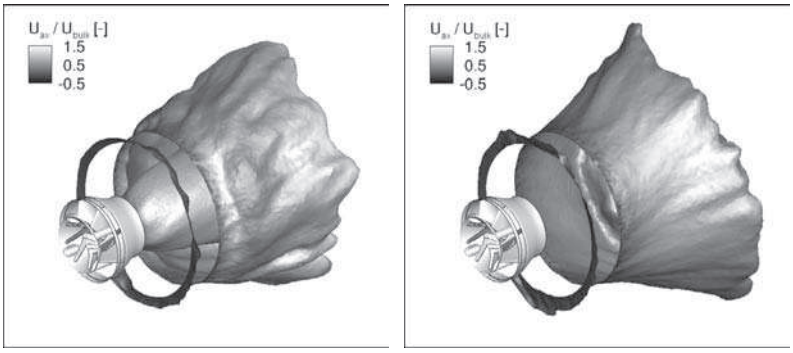

(a) *Attached* (b) *Detached*

Fig. 14. Temperature iso-surface ($T/T_{mean} = 1.3$) colored by normalized axial velocity for operating point 2: *Attached* (a) and *Detached* (b) flame.

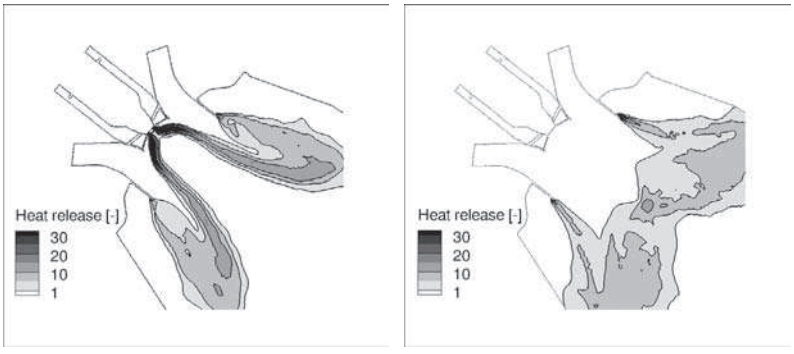

(a) *Attached* (b) *Detached*

Fig. 15. Heat release field on the middle cut plane (mean fields).

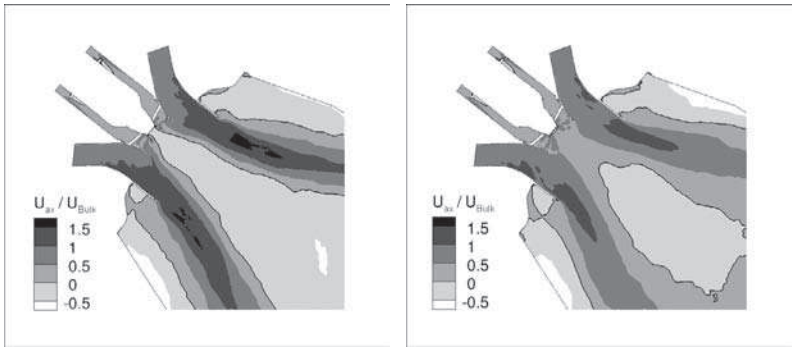

(a) *Attached* (b) *Detached*

Fig. 16. Axial velocity field and zero axial velocity iso-lines on the middle cut plane (mean fields).

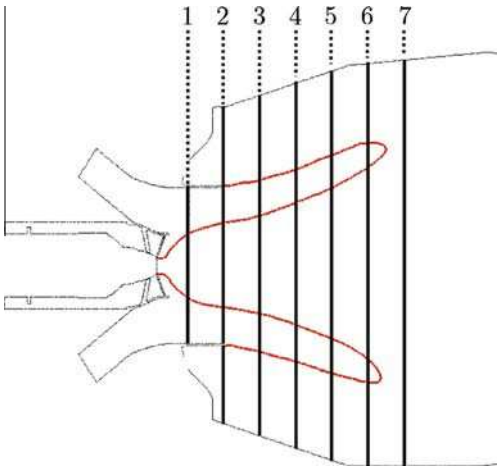

Fig. 17. Positions of profile extraction.

6.2. Instantaneous flow fields

During the initialisation of the operating condition 2, LES revealed that when the transition between the two states (operating point 1 to operating point 2) is applied suddenly, the flame detaches from the bluff body and a PVC develops, preventing the flame to move back to its normal stabilization point. Figure 24(a) and (b) use a low pressure iso-surface to represent the PVC and a temperature iso-line of $T/T_{mean} = 1.3$ to track the flame surface in 2D for the *Attached* and *Detached* flames, respectively. In the *Attached* case no PVC is present, whereas the *Detached* flame features a "finger-like" rotating structure in the inner region around which the PVC is turning (Fig. 24). The very large values of k (Fig. 21) near the bluff body for the *Detached* case are due to the strong PVC which develops in the cold gases in this zone. A similar phenomenon was observed by Staffelbach [13] who showed that the flame detaches with decreasing fuel mass flow rate at the bluff body.

7. Forced flames

It is interesting to investigate the response of both flames to an acoustic perturbation, since the flame position can have important effects on the time response and therefore on the stability of the machine (Rayleigh criterion [4,61]).

The FTFs measured for these swirled flames are shown in Fig. 25 over the Strouhal number (based on the bulk velocity and the burner diameter) and exhibit typical shapes observed in previous studies [29,33,34,39]. The gain in the *Attached* case is highest at frequency f_1 and is of the order of one. At f_2 the gain is already significantly lower and continues decreasing to $n = 0.5$ at f_4. The *Detached* flame gives similar amplitude responses to a perturbation at f_1, then decreases slightly at f_2 followed by a strong increase for higher frequencies reaching $n = 1.8$ at f_4. At frequency f_4, the *Detached* flame is much more sensitive to forcing than the *Attached* flame and more prone to inducing combustion instability. The

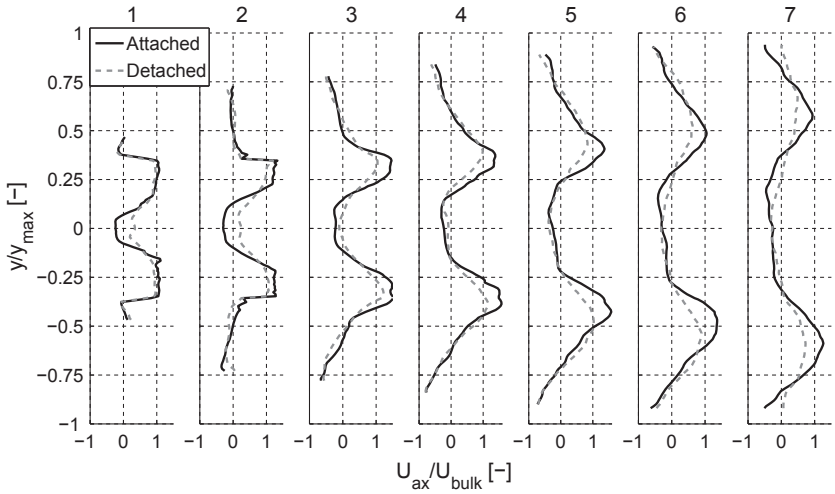

Fig. 18. Axial velocity profiles for the *Attached* and *Detached* flame (mean fields).

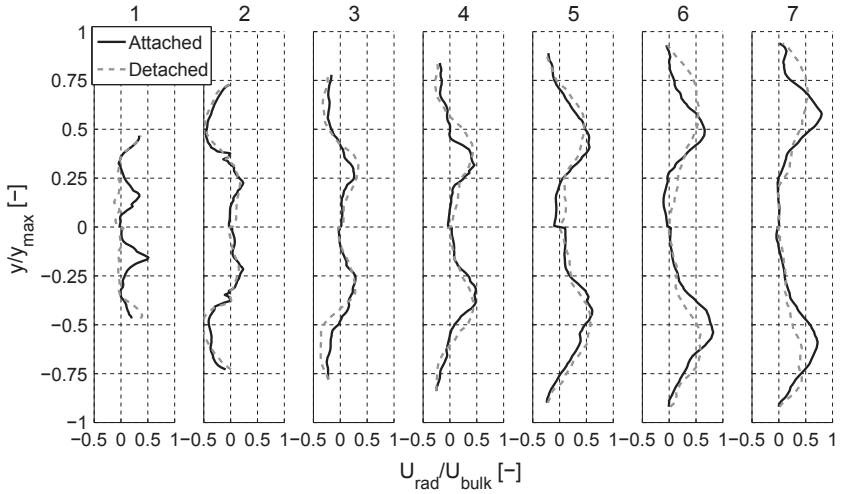

Fig. 19. Radial velocity profiles for the *Attached* and *Detached* flame (mean fields).

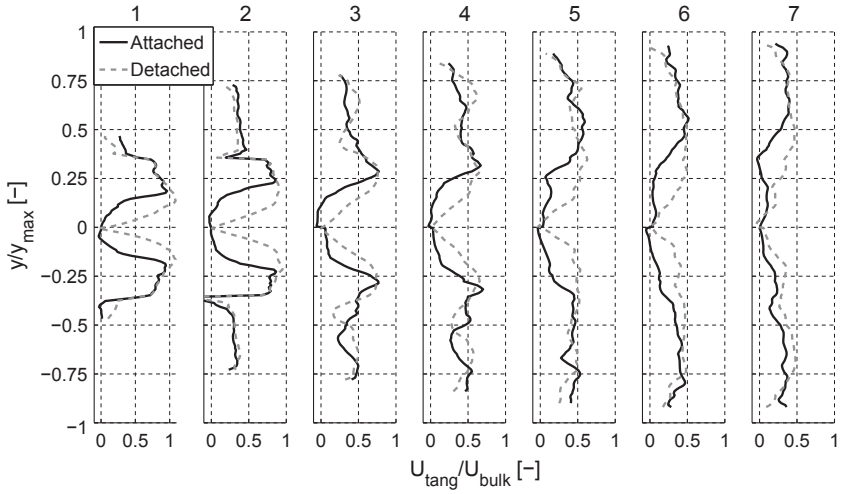

Fig. 20. Tangential velocity profiles for the *Attached* and *Detached* flame (mean fields).

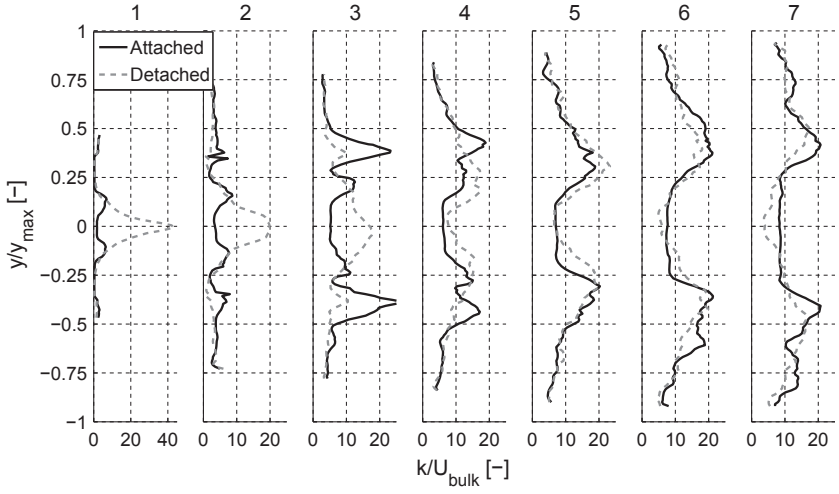

Fig. 21. Turbulent kinetic energy profiles for the *Attached* and *Detached* flame (mean fields).

phase of the FTF is also very different for both flames: it is decreasing with frequency in both cases, but the *Detached* flame is responding later for f_1, f_2 and f_4 than the *Attached* case.

Figure 25 demonstrates that thermoacoustic stability will be very different for both states: predicting stability using the FTF of one state or another one will obviously lead to different conclu-

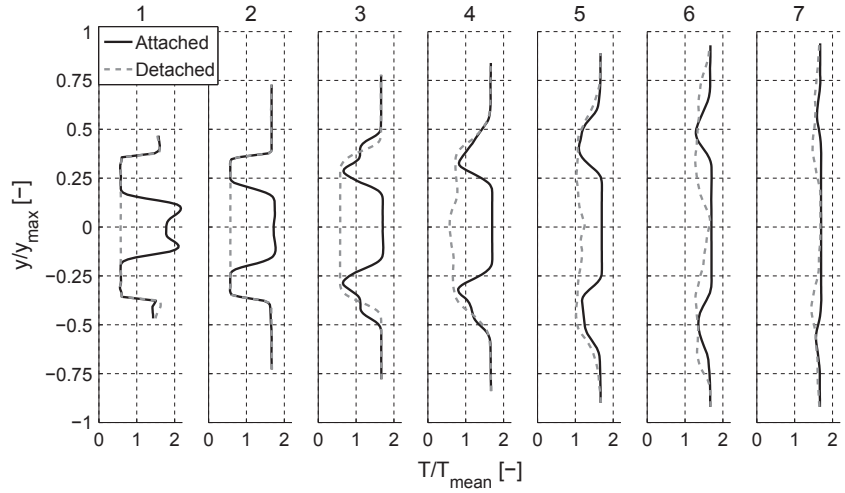

Fig. 22. Temperature profiles for the *Attached* and *Detached* flame (mean fields).

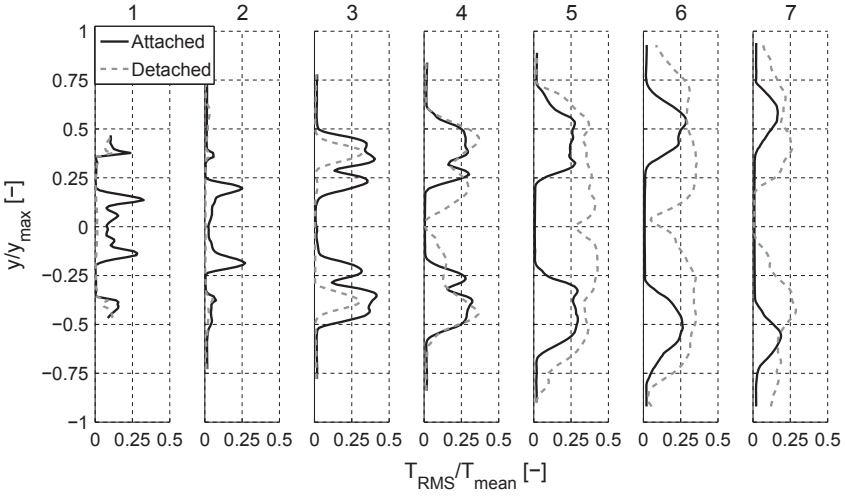

Fig. 23. RMS temperature profiles for the *Attached* and *Detached* flame (mean fields).

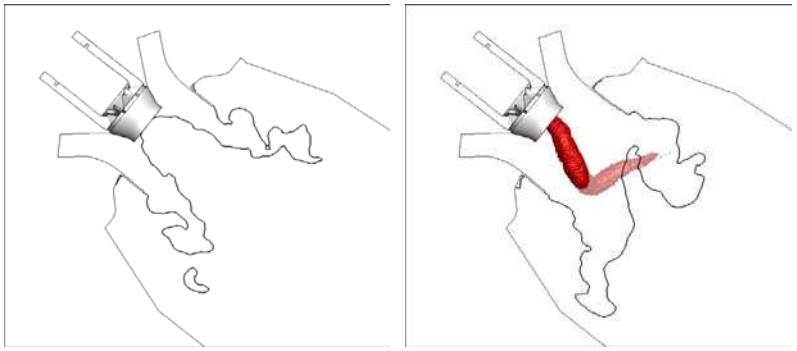

(a) *Attached* (b) *Detached*

Fig. 24. Temperature iso-line ($T/T_{mean} = 1.3$) and pressure iso-surface (visualizing the PVC structure): *Attached* (a) and *Detached* (b) flame (instantaneous fields). The PVC disappears for *Attached* (a), but it is strong for *Detached* (b).

sions. Moreover, the flame states themselves may also be sensitive to oscillations as shown in the next section. For example, the flame might be in state 1, become unstable, then change to state 2 which may be stable. This type of behavior can lead to non-harmonic limit cycles as shown by Boudy [62].

8. Bifurcation due to a change in fuel flow rate

It is of particular interest to know how the flame can transition from one state to the other. One way to do so in the real experiment, is to change the fuel mass flow rate in the pilot injection.

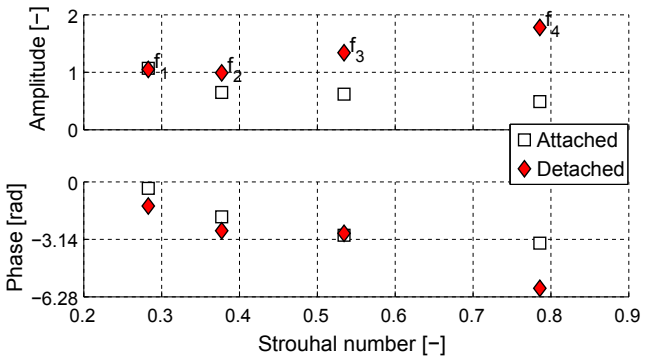

Fig. 25. Flame Transfer Function for frequencies f_1, f_2, f_3 and f_4 at $u'/\bar{u} = 0.06$.

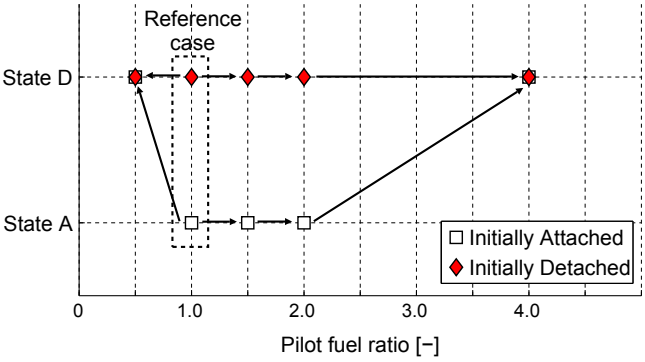

Fig. 26. Bifurcation diagram for the *Initially Attached* and *Initially Detached* states. The pilot fuel mass flow rate is varied and two states A (*Attached*) and D (*Detached*) exist.

The mean pilot fuel injection is a very sensitive control parameter controlling the flame position and its stability as shown for example by Hermann et al. [63] who used it to develop active control systems for thermoacoustics. The pilot fuel ratio (*pfr*) is introduced to measure the ratio of fuel flow rates in the LES and in the reference LES of operating point 2 *Attached* and *Detached*. Pilot fuel ratios of 0.5, 1.5, 2.0 and 4.0 are investigated, whereas $pfr = 1.0$ corresponds to the reference *Attached* and *Detached* states, respectively which is also the starting point of the hysteresis loop. All other parameters are kept constant. The hysteresis diagram is shown in Fig. 26. The *Initially Detached* flame stays detached with decreasing pilot fuel mass flow rate ($pfr = 0.5$), but it does not re-attach when the pilot fuel ratio is increased to 4.0. The *Initially Attached* flame however, detaches when the pilot fuel ratio is decreased to 0.5 which is in agreement with Staffelbach [13] who discovered in a similar case that the flame detaches from the bluff body with decreasing pilot fuel mass flow rate. The *Initially Attached* flame stays then on path D and cannot be re-attached anymore by an increase in pilot fuel mass flow rate. For *pfr* values up to 2.0, the *Initially Attached* case stays on path A, but detaches when the pilot fuel ratio reaches 4.0. In this case, the fuel mass flow rate injected in the pilot gas nozzle is very high, and leads to a detachment of the flame, showing that the flame stabilization in the *Attached* regime is difficult to maintain.

9. Bifurcation due to a change of the pulsation amplitude

Paschereit et al. [12] and Moeck et al. [15] found that acoustic forcing can lead to a suppression of the PVC. This point is investigated here. Only the highest frequency f_4 is considered and four different forcing amplitudes, 6%, 15%, 30% and 45% of the mean velocity at the diagonal inlet, are tested for both cases. The flow state evolves along two paths A (*Attached*) and D (*Detached*) shown in Fig. 27. Under forcing, the *Initially Attached* flame remains attached to the bluff body for all forcing amplitudes. However, *Initially Detached* stays on state D with pulsation up to 15% and moves to state A when the forcing amplitudes reaches 30% of the mean diagonal inlet velocity. In other words, state D which has the largest FTF amplitudes also comes back to state A if the oscillation amplitude becomes large.

To illustrate the attachment process, the relative heat release fluctuation $(q'/\bar{q})$ and the relative velocity fluctuation $(u'/\bar{u})$ at reference point A (Fig. 1) are shown in Fig. 28. Time is normalized by the forcing period T for f_4. The pulsation amplitude is 45%. Instantaneous snapshots of temperature in Fig. 29 show the attachment of the flame for distinct time steps, d1 to d4, for one oscillation cycle where the flame is detached (see Fig. 28), t1 to t8 for a "transition" of two oscillation cycles before the flame reattaches, and the first oscillation cycle of the *Attached* flame a1 to a4.

The pulsation is introduced at $t/T = 0$ and the flame starts oscillating at $t/T = 1$ almost in phase with the velocity fluctuation. Here, the flame is detached and the flame tip rolls up strongly forming a mushroom-like shape (d1 to d4 in Fig. 29). From $t/T = 2.8$ on, the relative heat release shows strong peaks for the following two oscillation periods. This is a transition period, where the flame starts moving in the direction bluff body due to rapidly decreasing relative velocity (t2). The heat release shows a high peak, as the flame starts interacting with the rich mixture injected at the pilot fuel evidenced by the high temperature region at t2. As the velocity increases again, the flame gets pushed away from the bluff body again (t3 and t4), but reattaches during the next oscillation cycle

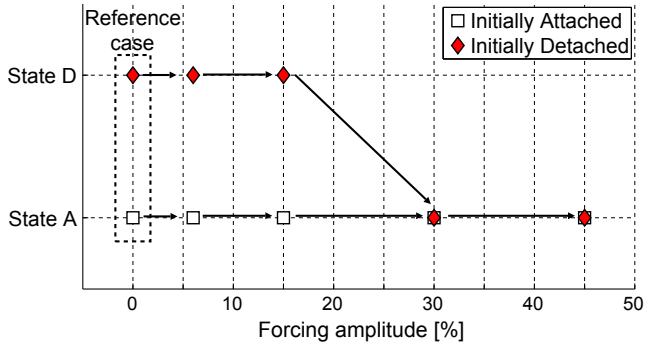

Fig. 27. Bifurcation diagram for the *Initially Attached* and *Initially Detached* flame. The forcing amplitude is varied and two states A (*Attached*) and D (*Detached*) exist.

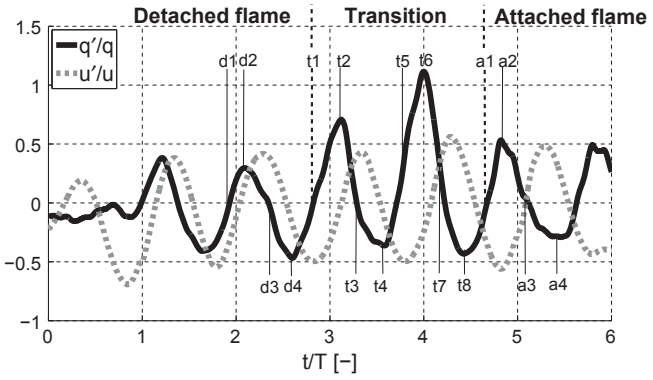

Fig. 28. Relative heat release and axial velocity fluctuation (reference point A) during the attachment of the *Detached* flame for f_4 at a pulsation amplitude of 45%.

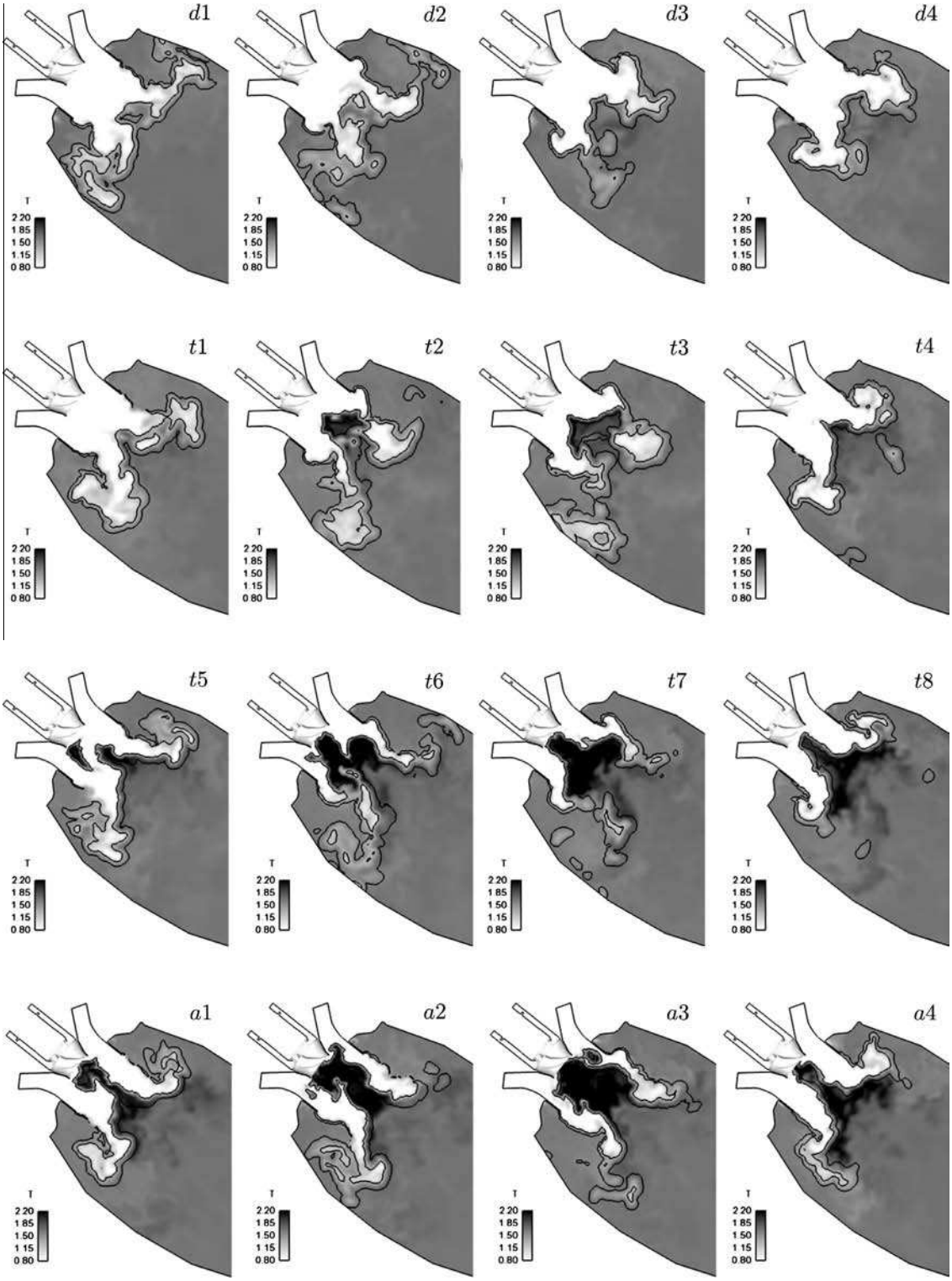

Fig. 29. Normalized temperature field on the middle cut plane for distinct snapshots during the attachment of the *Detached* flame for f_4 at a pulsation amplitude of 45%.

(t5 to t8). At the maximum heat release (peak at t6) the flame rolls up at the tip. A high flame surface appears and a rich mixture is burnt at the bluff body leading to this strong peak. In this transition period, the phase between relative axial velocity and relative heat release fluctuations change significantly and becomes out-of phase when the flame attaches at $t/T = 4.5$ (a1). This phase difference corresponds to the phase found for the pulsated *Attached* flame at lower pulsation amplitude in Section 7 (Fig. 25).

10. Conclusions

This study uses LES in a large scale swirled combustion chamber to study the relationships between Precessing Vortex Cores, bifurcations and thermoacoustics. Results can be summarized as follows: (1) in certain chambers, like the one studied here, the swirling flame can have two different states for the same regime: one where the flame is *Attached* to the burner exit and no PVC

can develop (state *Attached*) and a second one where the flame is lifted and a PVC develops between the swirler exit and the flame base (state *Detached*); (2) the Flame Transfer Functions, measured by forcing both flame states with acoustic waves, are very different for the *Attached* and the *Detached* states, suggesting different thermoacoustics effects. The *Detached* flame exhibits a larger response amplitude and a different time delay, compared to the standard *Attached* state; (3) the transition from *Attached* to *Detached* flame can be triggered by decreasing the pilot fuel flow rate, but the inverse transition from *Detached* to *Attached* cannot be obtained by increasing the pilot fuel flow rate. However, submitting the flames to acousting forcing reveals that the *Detached* flame can be forced to reattach when the forcing amplitude is large. These results can explain the complex behavior observed in certain gas turbines where the flame may trigger different acoustic responses for the same regime or oscillate between *Attached* and *Detached* states when strong oscillations are produced.

Acknowledgments

The authors acknowledge the support of Ansaldo Energia S.p.A. and of the EC through the Marie Curie Actions Networks for Initial Training program, under call FP7-PEOPLE-2007-1-1-ITN, Project LIMOUSINE with Project Number 214905 and CINES.

References

[1] P. Billant, J.-M. Chomaz, P. Huerre, J. Fluid Mech. 376 (1998) 183–219.
[2] O. Lucca-Negro, T. O'Doherty, Prog. Energy Comb. Sci. 27 (2001) 431–481.
[3] H. Liang, T. Maxworthy, J. Fluid Mech. 525 (2004) 115–159.
[4] L. Rayleigh, Nature 18 (1878) 319–321.
[5] M.G. Hall, Ann. Rev. Fluid Mech. 4 (1972) 195–217.
[6] L. Selle, G. Lartigue, T. Poinsot, R. Koch, K.-U. Schildmacher, W. Krebs, B. Prade, P. Kaufmann, D. Veynante, Combust. Flame 137 (4) (2004) 489–505.
[7] S. Roux, G. Lartigue, T. Poinsot, U. Meier, C. Bérat, Combust. Flame 141 (2005) 40–54.
[8] A. Giauque, L. Selle, T. Poinsot, H. Buechner, P. Kaufmann, W. Krebs, J. Turb. 6 (21) (2005) 1–20.
[9] A. Sengissen, J.F.V. Kampen, R. Huls, G. Stoffels, J.B.W. Kok, T. Poinsot, Combust. Flame 150 (2007) 40–53.
[10] Y. Huang, V. Yang, Prog. Energy Comb. Sci 35 (2009) 293–364.
[11] N. Syred, Prog. Energy Comb. Sci. 32 (2) (2006) 93–161.
[12] C.O. Paschereit, E. Gutmark, W. Weisenstein, AIAA J. 38 (6) (2000) 1025–1034.
[13] G. Staffelbach, Simulation aux grandes échelles des instabilités de combustion dans les configurations multi-brûleurs, PhD thesis, INP Toulouse, 2006.
[14] D. Galley, S. Ducruix, F. Lacas, D. Veynante, Combust. Flame 158 (2011) 155–171.
[15] J. Moeck, J.-F. Bourgouin, D. Durox, T. Schuller, S. Candel, Combust. Flame 159 (2012) 2650–2668.
[16] M. Stoehr, R. Sadanandan, W. Meier, Exp. Fluids 51 (2011) 1153–1167.
[17] T. Poinsot, D. Veynante, Theoretical and Numerical Combustion, third ed., R.T. Edwards, 2011.
[18] W. Krebs, P. Flohr, B. Prade, S. Hoffmann, Combust. Sci. Tech. 174 (2002) 99–128.
[19] R. Kaess, W. Polifke, T. Poinsot, N. Noiray, D. Durox, T. Schuller, S. Candel, in: Proceedings of the Summer Program, Center for Turbulence Research, NASA AMES, Stanford University, USA, 2008, pp. 289–302.
[20] P. Wolf, G. Staffelbach, A. Roux, L. Gicquel, T. Poinsot, V. Moureau, C. R. Acad. Sci. Méc. 337 (6–7) (2009) 385–394.
[21] L. Crocco, J. Am. Rocket Soc. 21 (1951) 163–178.
[22] L. Crocco, J. Am. Rocket Soc. 22 (1952) 7–16.
[23] S. Stow, A. Dowling, in: ASME Turbo Expo 2004-Power for Land Sea and Air, vol. GT2004-54245, Vienna, Austria, 2004.
[24] N. Noiray, D. Durox, T. Schuller, S. Candel, Combust. Flame 145 (3) (2006) 435–446.
[25] S. Thumuluru, H. Ma, T. Lieuwen, in: 45th AIAA Aerospace Sciences Meeting and Exhibit, AIAA Paper 2007-0845, Reno, USA, 2007.
[26] T. Schuller, D. Durox, S. Candel, Combust. Flame 134 (2003) 21–34.
[27] D. Durox, T. Schuller, S. Candel, in: Proceedings of the Combustion Institute, vol. 30, 2005, pp. 1717–1724.
[28] C.A. Armitage, R. Balachandran, E. Mastorakos, R. Cant, Combust. Flame 146 (2006) 419–436.
[29] V. Kornilov, R. Rook, J. ten Thije Boonkkamp, L. de Goey, Combust. Flame (2009) 1957–1970.
[30] D. Straub, G. Richards, in: ASME Paper 99-GT-109, 1999.
[31] C. Hirsch, D. Franca, P. Reddy, W. Polifke, T. Sattelmayer, Influence of the swirler design on the flame transfer function of premixed flames, ASME Paper GT2005-68195, 2005.
[32] T. Komarek, W. Polifke, J. Eng. Gas Turb. Power 132 (6) (2010) 1–061503.
[33] P. Palies, D. Durox, T. Schuller, S. Candel, Combust. Flame 157 (2010) 1698–1717.
[34] P. Palies, T. Schuller, D. Durox, S. Candel, in: Proceedings of the Combustion Institute, vol. 33, 2011, pp. 2967–2974.
[35] T. Lieuwen, B.T. Zinn, Proc. Combust. Inst. 27 (1998) 1809–1816.
[36] B. Schuermans, V. Bellucci, F. Guethe, F. Meili, P. Flohr, C. Paschereit, in: ASME Turbo Expo 2004-Power for Land Sea and Air, vol. GT2004-53831, Vienna, Austria, 2004.
[37] A. Birbaud, S. Ducruix, D. Durox, S. Candel, Combust. Flame 154 (3) (2008) 356–367.
[38] K. Kim, J. Lee, B. Quay, D. Santavicca, Combust. Flame 157 (2010) 1731–1744.
[39] D. Durox, T. Schuller, N. Noiray, S. Candel, in: Proceedings of the Combustion Institute, vol. 32, 2009, pp. 1391–1398.
[40] A.K. Gupta, D.G. Lilley, N. Syred, Swirl Flows, Abacus Press, 1984.
[41] A. Steinberg, I. Boxx, M. Stoehr, C. Carter, W. Meier, Combust. Flame 157 (2010) 2250–2266.
[42] L. Tay-Wo-Chong, W. Polifke, ASME J. Eng. Gas Turb. Power 135 (2013) 021502.
[43] O. Stein, A. Kempf, Proc. Combust. Inst. 31 (2007) 1755–1763.
[44] G. Staffelbach, L. Gicquel, G. Boudier, T. Poinsot, Proc. Combust. Inst. 32 (2009) 2909–2916.
[45] C. Sensiau, F. Nicoud, T. Poinsot, Int. J. Aeroacoust. 8 (1) (2009) 57–68.
[46] T. Schønfeld, M. Rudgyard, AIAA J. 37 (11) (1999) 1378–1385.
[47] C. Hirsch, Numerical Computation of Internal and External Flows, vol. 2, John Wiley & Sons, New York, 1990.
[48] P.D. Lax, B. Wendroff, Commun. Pure Appl. Math. 13 (1960) 217–237.
[49] J. Smagorinsky, Mon. Weather Rev. 91 (1963) 99–164.
[50] B. Franzelli, E. Riber, L. Gicquel, T. Poinsot, Combust. Flame 159 (2012) 621–637.
[51] O. Colin, F. Ducros, D. Veynante, T. Poinsot, Phys. Fluids 12 (7) (2000) 1843–1863.
[52] O. Colin, M. Rudgyard, J. Comput. Phys. 162 (2) (2000) 338–371.
[53] J.-P. Légier, T. Poinsot, D. Veynante, in: Proc. of the Summer Program, Center for Turbulence Research, NASA Ames/Stanford Univ., 2000, pp. 157–168.
[54] F. Charlette, D. Veynante, C. Meneveau, Combust. Flame 131 (2002) 159–180.
[55] T. Poinsot, S. Candel, J. Comput. Phys. 62 (1986) 282–296.
[56] G. Boudier, L.Y.M. Gicquel, T. Poinsot, D. Bissières, C. Bérat, Combust. Flame 155 (1–2) (2008) 196–214.
[57] P. Wolf, G. Staffelbach, L. Gicquel, J.-D. Müller, T. Poinsot, Combust. Flame 159 (2012) 3398–3413.
[58] T. Poinsot, S. Lele, J. Comput. Phys. 101 (1) (1992) 104–129.
[59] P. Schmitt, T. Poinsot, B. Schuermans, K.P. Geigle, J. Fluid Mech. 570 (2007) 17–46.
[60] A. Kaufmann, F. Nicoud, T. Poinsot, Combust. Flame 131 (2002) 371–385.
[61] F. Nicoud, T. Poinsot, Combust. Flame 142 (2005) 153–159.
[62] F. Boudy, D. Durox, T. Schuller, S. Candel, in: Proceedings of the Combustion Institute, vol. 33, 2011, pp. 1121–1128.
[63] J. Hermann, A. Orthmann, S. Hoffmann, P. Berenbrink, Combination of active instability control and passive measures to prevent combustion instabilities in a 260 mw heavy duty gas turbine, Braunschweig, Germany, 2000.